# Finite-volume and partial quenching effects in the magnetic polarizability of the neutron

J. M. M. Hall,[1] D. B. Leinweber,[1] and R. D. Young[1,2]

[1]*Special Research Centre for the Subatomic Structure of Matter (CSSM),*
*School of Chemistry and Physics, University of Adelaide, Adelaide, South Australia 5005, Australia*
[2]*ARC Centre of Excellence for Particle Physics at the Terascale,*
*School of Chemistry and Physics, University of Adelaide, Adelaide, South Australia 5005, Australia*

There has been much progress in the experimental measurement of the electric and magnetic polarizabilities of the nucleon. Similarly, lattice QCD simulations have recently produced dynamical QCD results for the magnetic polarizability of the neutron approaching the chiral regime. In order to compare the lattice simulations with experiment, calculation of partial quenching and finite-volume effects is required prior to an extrapolation in quark mass to the physical point. These dependencies are described using chiral effective field theory. Corrections to the partial quenching effects associated with the sea-quark-loop electric charges are estimated by modeling corrections to the pion cloud. These are compared to the uncorrected lattice results. In addition, the behavior of the finite-volume corrections as a function of pion mass is explored. Box sizes of approximately 7 fm are required to achieve a result within 5% of the infinite-volume result at the physical pion mass. A variety of extrapolations are shown at different box sizes, providing a benchmark to guide future lattice QCD calculations of the magnetic polarizabilities. A relatively precise value for the physical magnetic polarizability of the neutron is presented, $\beta^n = 1.93(11)^{\text{stat}}(11)^{\text{sys}} \times 10^{-4} \text{ fm}^3$, which is in agreement with current experimental results.

## I. INTRODUCTION

The study of the electric and magnetic polarizabilities of the nucleon is a topic of intense ongoing interest. Although measurement of the sum of the polarizabilities from Compton scattering has been achieved experimentally for some time [1,2], a direct determination of the individual electric and magnetic polarizabilities still presents a challenge, with uncertainties remaining large [3–6]. In the case of the neutron, recent values of $\beta^n$ include $4.1 \pm 2.0$ [6], $3.7 \pm 2.0$ [7] and $2.7^{+2.2}_{-2.4}$ [3,4], in units of $10^{-4} \text{ fm}^3$.

Recent improvements in lattice QCD techniques in the treatment of Landau levels [8] and the simulation of uniform magnetic fields with improved boundary conditions [9,10] offer new insights into the polarizabilities of the nucleon. When comparing lattice results with experiment, care must be taken in extrapolating the results to the chiral limit while incorporating finite-volume effects. The latter have been shown to be significant even at modern lattice volumes [11–17].

Chiral perturbation theory ($\chi$PT) represents an important tool for performing chiral extrapolations of lattice results to the physical point. Though lattice simulations are now approaching the chiral regime [18–25], multiple pion-mass points must be used to constrain the parameters of the extrapolation. These data sets typically extend outside the chiral power-counting regime (PCR) of $\chi$PT. It has been demonstrated that use of $\chi$PT outside its region of applicability leads to incorrect results [26,27]. Therefore, an extension of chiral effective field theory ($\chi$EFT) with improved convergence properties will be used. The approach incorporates a resummation of the higher-order terms of the chiral expansion, while being exactly equivalent to $\chi$PT within the power-counting regime [26,27]. The size of the total contribution from the higher-order terms is determined by a finite-valued energy scale which has been linked to the intrinsic scale associated with the size of the hadron under investigation [28,29].

In this paper, the focus is on the magnetic polarizability of the neutron, and connect recent lattice QCD results from the CSSM [9,10] to contemporary experimental results, providing a sound comparison of theory and experiment. The lattice QCD results are founded on the PACS-CS configurations [19] made available via the International Lattice Data Grid (ILDG) [30]. These dynamical QCD results from the simulation are analyzed using $\chi$EFT. A particular difficulty, addressed in this paper, is that the best lattice QCD results have yet to incorporate the contributions from photon couplings to sea-quark loops comprising the meson dressings of $\chi$EFT. Our choice of regularization scheme facilitates the modeling of the corrections [31] associated with these effects.

In the following sections, the methods of unquenching, finite-volume corrections, and chiral extrapolations are established, and a prediction for the magnetic polarizability of the neutron is reported. This prediction is complemented by a variety of finite-volume extrapolations at different box

sizes, providing a benchmark to guide future lattice QCD calculations of the magnetic polarizabilities.

## II. LATTICE QCD

In calculating the magnetic polarizability in lattice QCD, a background magnetic field $B$ is introduced on the lattice by multiplying each gauge link by a certain phase factor [9,10,32–37]. In the weak-field limit, the resultant energy shift of the nucleon is dependent on the magnetic moment $\vec{\mu}$, and the magnetic polarizability $\beta$, through

$$E(B) = M_N - \vec{\mu} \cdot \vec{B} + \frac{e|B|}{2M_N} - 2\pi\beta B^2 + O(B^3). \quad (1)$$

The period boundary conditions restrict the possible values of the magnetic field strength, based on the number of lattice sites $N_x$ and $N_y$ in the $x$ and $y$ directions, leading to the quantization condition

$$qBa^2 = \frac{2\pi n}{N_x N_y}, \qquad n \in \mathbb{Z}, \quad (2)$$

for a quark charge $q$.

The background field method is applied to the PACS-CS configurations [19] obtained via the ILDG [30], which use the $2+1$ flavor improved clover fermion action and the Iwasaki gauge action. The lattice results used in this analysis are presented in Fig. 1, utilizing the Sommer scale parameter [38], $r_0 = 0.49$ fm [9,10]. Note that all the lattice points considered satisfy $m_\pi L > 4.45$ such that the use of finite-volume $\chi$EFT in analyzing these results is appropriate.

In computing the polarizabilities, contributions from photon couplings to disconnected sea-quark loops have
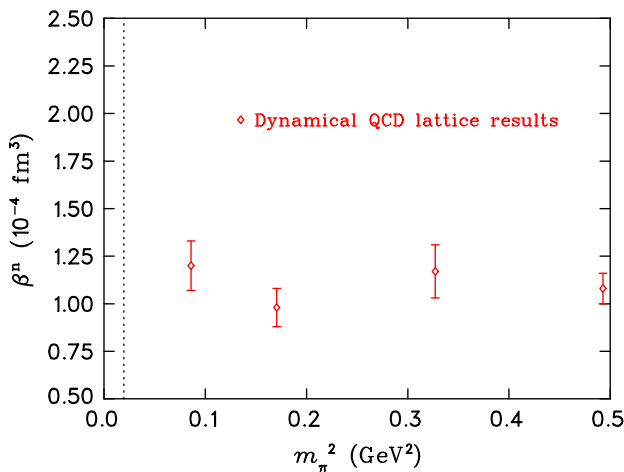


FIG. 1 (color online). The magnetic polarizability of the neutron $\beta^n$, from $2+1$ flavor lattice QCD simulations by the CSSM [9,10]. The results are based on the PACS-CS configurations [19] available via the ILDG [30].

not yet been included. These need to be accounted for prior to making a comparison with experimental results. In the case of the neutron, partially quenched $\chi$EFT is used to determine the appropriate chiral behavior of the polarizability in both the partially quenched scenario of the lattice results and full QCD.

Other calculations of the magnetic polarizability of the neutron [35,37] use a different approach. While the linearization of the U(1) field breaks gauge invariance [10], the main concern in this alternative data set is the use of the Dirichlet boundary condition in a spatial direction breaking the symmetry of the 3-torus, which may give rise to significant systematic errors due to artifacts at the boundary. Since finite-volume $\chi$EFT employs periodic boundary conditions in all spatial directions, these lattice results are not compatible with the formalism, and are therefore not used in this investigation.

## III. CHIRAL EFFECTIVE FIELD THEORY

The electric and magnetic polarizabilities $\alpha$ and $\beta$, respectively, may be defined in terms of two independent parameters, $(A, B)$, obtained from expanding the Compton tensor [1],

$$T_{\mu\nu}(p, q) = \int d^4 x e^{iq \cdot x} \langle N(p)| T\{J_\mu^{\mathrm{em}}(x) J_\nu^{\mathrm{em}}(0)\} |N(p)\rangle. \quad (3)$$

They are defined as

$$\alpha + \beta = -\frac{e^2 m}{2\pi} \frac{\partial^2 A(s)}{\partial s^2}\bigg|_{s=m^2}, \qquad \beta = -\frac{e^2}{4\pi m} B(s = m^2). \quad (4)$$

The interaction vertices are sourced from the relevant first-order interaction Lagrangian of heavy-baryon $\chi$PT, which includes the $\Delta$ baryon transitions [39,40]

$$L_{\mathrm{HB\chi PT}}^{(1),\mathrm{int}} = i\frac{g_A}{2f_\pi} \bar{\Psi}_v \gamma_5 \sigma_{\mu\nu} v^\nu \tau^a \partial^\mu \pi^a \Psi_v$$
$$+ i\frac{C}{2f_\pi} \bar{\Psi}_v T^a \sigma_{\mu\nu} \Delta_v^\nu \partial^\mu \pi^a + \mathrm{H.c.} \quad (5)$$

$T^a$ are the isospin doublet-quartet transition matrices. The octet couplings $D$ and $F$ are derived from the experimental value of $g_A$, obeying the condition $D + F = g_A$ and the $SU(6)$ symmetry relation $F = \frac{2}{3}D$.

The calculation of the leading-order loop contributions follows Refs. [31,41] and uses the heavy-baryon approximation. In the finite-range regularization approach, the leading nonanalytic contribution to the chiral expansion comes entirely from the diagram shown in Fig. 2, for the above parametrization of $\beta^n$ (contributing to $A_2$ from Ref. [6]). Transitions to a $\Delta$ baryon at leading order are
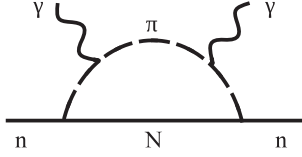
FIG. 2.    The leading-order pion loop contribution to the magnetic polarizability of the neutron.

shown in Fig. 3. For a finite mass-splitting $\Delta$, Fig. 3 contributes a log term rather than $1/m_\pi$ [41].

By performing the pole integration over $k_0$ and taking the forward scattering limit ($q \cdot q' \to 0$), one obtains a three-dimensional integral form that can easily be adapted to estimate finite-volume corrections [28,42,43]

$$\beta^{(\pi N)}(m_\pi^2) = \frac{e^2}{4\pi} \frac{1}{288\pi^3 f_\pi^2} \chi_N \int \mathrm{d}^3 k \frac{\vec{k}^2}{(\vec{k}^2 + m_\pi^2)^3}, \quad (6)$$

$$\beta^{(\pi \Delta)}(m_\pi^2) = \frac{e^2}{4\pi} \frac{1}{288\pi^3 f_\pi^2} \chi_\Delta \int \mathrm{d}^3 k$$
$$\times \frac{\omega_{\vec{k}}^2 \Delta(3\omega_{\vec{k}} + \Delta) + \vec{k}^2(8\omega_{\vec{k}}^2 + 9\omega_{\vec{k}}\Delta + 3\Delta^2)}{8\omega_{\vec{k}}^5(\omega_{\vec{k}} + \Delta)^3}, \quad (7)$$

where $\omega_{\vec{k}} = \sqrt{\vec{k}^2 + m_\pi^2}$ is the energy carried by the pion with three-momentum $\vec{k}$, $\Delta \equiv M_\Delta - M_N = 292$ MeV, and the pion decay constant is taken to be $f_\pi = 92.4$ MeV. The standard coefficients for full QCD are given by

$$\chi_N = 2g_A^2, \quad (8)$$

$$\chi_\Delta = \frac{16}{9} C^2, \quad (9)$$

with the coupling constants taking the values $g_A = 1.267$, $C = -1.52$. Modifications to the couplings to accommodate partial quenching effects are explained in Sec. III A.

The leading-order $1/m_\pi$ contribution to the magnetic polarizability of the neutron has the established coefficient [44–46]

$$\beta^{\pi N}(m_\pi^2) = \frac{e^2 g_A^2}{768\pi^2 f_\pi^2} \frac{1}{m_\pi} \equiv \chi' \frac{1}{m_\pi}. \quad (10)$$
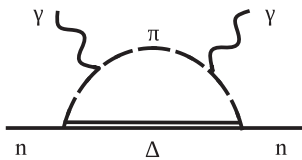


FIG. 3.    The leading-order pion loop contribution to the magnetic polarizability of the neutron, allowing transitions to nearby and strongly coupled $\Delta$ baryons.

The chiral expansion of the magnetic polarizability of the neutron at this order is

$$\beta^n = \frac{\chi'}{m_\pi} + c_0 - \frac{16}{9\Delta} \chi' \log(m_\pi/\mu) + O(m_\pi), \quad (11)$$

where $\mu$ is an arbitrary mass scale associated with the logarithm, henceforth set to 1 GeV.

Finite-volume effects are evaluated following the prescription described in Refs. [11,28,29]. These are estimated by evaluating the corrections associated with replacing the continuum integrals of Eqs. (6) and (7) with finite sums over the momenta available on the lattice. Using this method, the finite-volume corrections are stable for large values of the regularization scale and are numerically equivalent to the algebraic approach described in Refs. [47,48].

When applying $\chi$EFT to lattice QCD results, pion-mass values extending outside the chiral power-counting regime are typically considered, and use of standard $\chi$PT in this region inevitably leads to a badly divergent chiral series [26,27]. The identification of an intrinsic scale for the regularization of loop integrals provides a robust method for resumming the higher-order terms of the chiral expansion and calculating the low-energy coefficients of $\chi$PT [11,13,28,29].

In evaluating the loop integrals of the effective field theory, a dipole regulator, $u^2(k, \Lambda) = (1 + \vec{k}^2/\Lambda^2)^{-4}$, is introduced into the integrands to ensure only soft momenta flow through the effective field theory degrees of freedom. Through an examination of the flow of the low-energy coefficients constrained by the lattice QCD results as the regulator parameter, $\Lambda$ is varied, and with an understanding of the dependence of this flow on the range of pion masses considered in the chiral expansion, one can identify a value of $\Lambda$ which provides low-energy coefficients independent of the pion mass range considered, and are therefore consistent with the low-energy coefficients of $\chi$PT in the PCR [11,13,28,29,49].

A weighted average across studies of the leading-order chiral coefficients of the nucleon mass [28,50] (using PACS-CS results [19]), magnetic moment [11] and the electric charge radius [13] (using QCDSF results [21]) leads to a regulator parameter of $\bar{\Lambda}^{\text{scale}} = 0.99(27)$ GeV.

For the present case, the dipole regulator is introduced into the integrands of Eqs. (6) and (7). In light of our additional task of correcting for the partial quenching of the lattice QCD simulations, the value $\Lambda = 0.80$ GeV is adopted [40,51–55], in agreement with the intrinsic scale identified in previous studies [11,13,28,50]. This particular regulator mass has been shown to define a pion cloud contribution to masses [51], magnetic moments [52], and charge radii [40], which enables one to model the correction to the pion cloud encountered in unquenching and to reproduce experimental measurements. As explained in

Refs. [40,51–55], this particular choice of regulator parameter defines a neutron core contribution, which does not differ significantly between partially quenched QCD and full $2+1$ flavor QCD. In making this connection, one makes the model assumption that the core is insensitive to sea-quark loop contributions.

### A. Partially quenched chiral effective field theory

In this section, an independent calculation is presented for the calculation of the loop coefficients for partially quenched $\chi$PT. The approach is complementary to the graded-symmetry approach selected by Detmold *et al.* [31] and provides an alternative picture of the process based on standard nuclear physics processes. In addition, the unquenching procedure is outlined, which corrects the lattice simulation results to full QCD.

The procedure for obtaining the partially quenched $\chi$PT coefficients of nonanalytic terms follows that described in Ref. [56]. First, one separates the contribution from each quark-flow diagram into "valence-valence," "valence-sea," and "sea-sea" contributions. These describe whether the two photons couple to valence or sea quarks in the intermediate states available in Figs. 2 and 3.

Starting with $n \to N\pi$, and selecting the $n \to n\pi^0$ channel, one writes out all the possible quark-flow diagrams, prior to attaching external photons to the meson, as shown in Fig. 4. Diagram 4(a) contains only valence quarks, and therefore can only contribute to the valence-valence sector. Diagrams 4(b) and (c) may contribute to all three sectors, as one or both photons may be attached to the valence- or
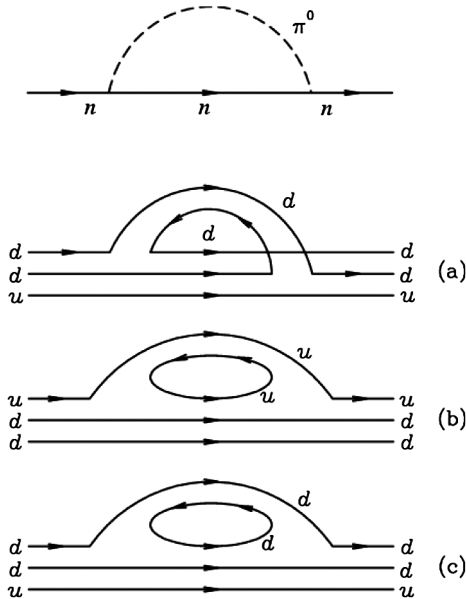


FIG. 4. Example: the decomposition of the process $n \to n\pi^0$ into its possible one-loop quark-flow diagrams. The configuration of photon couplings to valence and sea quarks will determine the coefficients of partially quenched $\chi$PT.

sea-quark lines of the intermediate meson. These occur in proportion to the quark charges.

While the neutrality of the $\pi^0$ meson ensures the total leading-order contribution is zero, this occurs through a combination of valence-valence, valence-sea, and sea-sea contributions, with the latter two omitted in the lattice QCD simulations. For example, in the case of diagram 4(b), the coupling of photons to either valence- or sea-quark lines generates

$$\chi_{nn\pi^0}^{\text{diag}(b)} \propto (q_u^2 + 2q_u q_{\bar{u}} + q_{\bar{u}}^2), \tag{12}$$

$$\propto (q_u + q_{\bar{u}})^2 = 0. \tag{13}$$

The three terms in Eq. (12) contribute to valence-valence, valence-sea and sea-sea, respectively. For quark charges $q_u = +2/3$, $q_{\bar{u}} = -2/3$, clearly the total contribution from $n \to n\pi^0$ vanishes, as expected.

Setting electric charges aside, the $SU(3)$ flavor coupling for diagram 4(b) alone is obtained by temporarily replacing the up-quark sea-quark-loop with a strange quark [56]. This correctly isolates the quark-flow diagram only containing a disconnected sea-quark-loop flow:

$$\chi_{nn\pi^0}^{\text{diag}(b)} \propto \chi_{K^+\Sigma^-}^2 = 2(D-F)^2. \tag{14}$$

By repeating the above procedure for diagram 4(c), one finds

$$\chi_{nn\pi^0}^{\text{diag}(c)} \propto (q_d^2 + 2q_d q_{\bar{d}} + q_{\bar{d}}^2), \tag{15}$$

$$\propto (q_d + q_{\bar{d}})^2 = 0, \tag{16}$$

and

$$\chi_{nn\pi^0}^{\text{diag}(c)} \propto \chi_{K^0\Sigma^0}^2 + \chi_{K^0\Lambda}^2$$

$$\propto (D-F)^2 + \frac{1}{3}(D+3F)^2. \tag{17}$$

As a result, one can now identify which components of the $n \to n\pi^0$ channel have a disconnected sea-quark loop in the quark flow. Monitoring the quark charges that couple to the photons enables one to identify the different valence-sea and sea-sea quark sectors. Thus, the valence-sea and sea-sea contributions can be calculated explicitly, as above. Knowing the total coefficient from standard $\chi$PT, the remainder represents the valence-valence contribution including the connected quark flow of diagram 4(a). One may also apply this procedure to the $n \to p\pi^-$ channel.

In order to obtain the total partially quenched result for $n \to N\pi$, one must also consider the unphysical process $n \to n^-\pi^+$. This process does not occur in full QCD since the propagation of negatively charged $ddd$ neutronlike states violates the Pauli exclusion principle. This is realized

TABLE I. The relative contributions to the leading-order loop integrals of Figs. 2 and 3. The numerical value of the couplings can be obtained by inserting the appropriate quark charges and noting $\chi^2_{K^+\Sigma^-} = 2(D-F)^2$, $\chi^2_{K^0\Sigma^0} = (D-F)^2$, and $\chi^2_{K^0\Lambda} = (D+3F)^2/3$ for the octet intermediate states, and $\chi^2_{K^+\Sigma^{*-}} = 4\,C^2/9$ and $\chi^2_{K^0\Sigma^{*0}} = 2\,C^2/9$ for decuplet intermediate states. The valence-valence sector can be calculated by subtracting the two other sectors from the total result.

| $\acute{n} \to N\pi$ | Total | Valence-sea | Sea-sea |
|---|---|---|---|
| $n \to n\pi^0$ | $0$ | $2q_u q_{\bar{u}} \chi^2_{K^+\Sigma^-} + 2q_d q_{\bar{d}}(\chi^2_{K^0\Sigma^0} + \chi^2_{K^0\Lambda})$ | $q^2_{\bar{u}}\chi^2_{K^+\Sigma^-} + q^2_{\bar{d}}(\chi^2_{K^0\Sigma^0} + \chi^2_{K^0\Lambda})$ |
| $n \to p\pi^-$ | $2(D+F)^2$ | $2q_d q_{\bar{u}}(\chi^2_{K^0\Sigma^0} + \chi^2_{K^0\Lambda})$ | $q^2_{\bar{u}}(\chi^2_{K^0\Sigma^0} + \chi^2_{K^0\Lambda})$ |
| $n \to n^-\pi^+$ | $0$ | $2q_u q_{\bar{d}}\chi^2_{K^+\Sigma^-}$ | $q^2_{\bar{d}}\chi^2_{K^+\Sigma^-}$ |
| $\acute{n} \to \Sigma K$ | | | |
| $n \to (\Sigma^0,\Lambda)K^0$ | $0$ | $2q_d q_{\bar{s}}(\chi^2_{K^0\Sigma^0} + \chi^2_{K^0\Lambda})$ | $q^2_{\bar{s}}(\chi^2_{K^0\Sigma^0} + \chi^2_{K^0\Lambda})$ |
| $n \to \Sigma^- K^+$ | $2(D-F)^2$ | $2q_u q_{\bar{s}}\chi^2_{K^+\Sigma^-}$ | $q^2_{\bar{s}}\chi^2_{K^+\Sigma^-}$ |
| $\acute{n} \to \Delta\pi$ | | | |
| $n \to \Delta^0\pi^0$ | $0$ | $2q_u q_{\bar{u}}\chi^2_{K^+\Sigma^{*-}} + 2q_d q_{\bar{d}}\chi^2_{K^0\Sigma^{*0}}$ | $q^2_{\bar{u}}\chi^2_{K^+\Sigma^{*-}} + q^2_{\bar{d}}\chi^2_{K^0\Sigma^{*0}}$ |
| $n \to \Delta^+\pi^-$ | $\frac{4}{9}\,C^2$ | $2q_d q_{\bar{u}}\chi^2_{K^0\Sigma^{*0}}$ | $q^2_{\bar{u}}\chi^2_{K^0\Sigma^{*0}}$ |
| $n \to \Delta^-\pi^+$ | $\frac{4}{3}\,C^2$ | $2q_u q_{\bar{d}}\chi^2_{K^+\Sigma^{*-}}$ | $q^2_{\bar{d}}\chi^2_{K^+\Sigma^{*-}}$ |
| $\acute{n} \to \Sigma^* K$ | | | |
| $n \to \Sigma^{*0} K^0$ | $0$ | $2q_d q_{\bar{s}}\chi^2_{K^0\Sigma^{*0}}$ | $q^2_{\bar{s}}\chi^2_{K^0\Sigma^{*0}}$ |
| $n \to \Sigma^{*-} K^+$ | $\frac{4}{9}\,C^2$ | $2q_u q_{\bar{s}}\chi^2_{K^+\Sigma^{*-}}$ | $q^2_{\bar{s}}\chi^2_{K^+\Sigma^{*-}}$ |

in full QCD by a cancellation of the two quark-flow diagrams associated with $n \to n^-\pi^+$. These diagrams are obtained from Figs. 4(a) and 4(b), with the change of the valence flavor labels $d, d, u$ to $u, d, d$. While the sum of these two diagrams vanishes, each one participates in the leading-order nonanalytic coefficients of the magnetic polarizability. An omission of photon couplings to the disconnected sea-quark loop in the lattice QCD simulations allows a nontrivial contribution. The cancellation no longer takes place, and this must be taken into account when fitting the lattice results.

The diagrammatic procedure may be repeated for $n \to \Delta\pi$. A summary of the contributions in different channels is shown in Table I for both octet and decuplet transitions. In summary, the modifications to the loop integrals of Eqs. (6) and (7) due to partial quenching in the lattice QCD simulations are

$$\chi_N \to \chi_N^{pQ} = 2g_A^2 - (D-F)^2 - \frac{7}{27}(D+3F)^2, \quad (18)$$

$$\chi_\Delta \to \chi_\Delta^{pQ} = \frac{16}{9}\,C^2 - \frac{2}{9}\,C^2. \quad (19)$$

Note that these coefficients are consistent with those derived from the graded-symmetry approach (see Table I of Ref. [31]).

Because the lattice simulations incorporate $2+1$ flavors, the kaon loops also require consideration. Given the international attention devoted to learning the strangeness contribution to the magnetic moment of the nucleon, it is fascinating to perform a similar calculation [52] for the magnetic polarizability. To achieve this, additional loop integrals are considered with the same form as Eq. (7) but with the pion replaced by the kaon and the mass splitting

associated with the increased mass of the hyperons in the intermediate states.

Specifically, the symbol $\Delta$ in Eq. (7) represents the mass splitting between the nucleon and either the $\Sigma$ or the $\Sigma^*$ baryon; taking the experimental charge-state averages, $m_\Sigma = 1.189$ GeV and $m_{\Sigma^*} = 1.383$ GeV. The kaon mass is related to the pion mass via

$$m_K^2 = m_{K,\text{phys}}^2 + \frac{1}{2}(m_\pi^2 - m_{\pi,\text{phys}}^2). \quad (20)$$

The coefficient for the partially strange quark contribution to the neutron magnetic moment is obtained with the modification of $\chi_\Delta$ in Eq. (7),

$$\chi_\Delta \to \chi_{K\Sigma}^{pQ} = 2(D-F)^2 - (D-F)^2 + \frac{1}{27}(D+3F)^2 \quad (21)$$

and

$$\chi_\Delta \to \chi_{K\Sigma}^{pQ} = \frac{4}{9}\,C^2 - \frac{2}{9}\,C^2, \quad (22)$$

where the first term on the right-hand side of these equations is the full QCD contribution.

The strange sea-quark-loop contribution to the nucleon magnetic polarizabilities can be obtained via

$$\chi_\Delta \to \chi_{K\Sigma}^{s} = \frac{1}{3}(D-F)^2 + \frac{1}{27}(D+3F)^2 \quad (23)$$

and

$$\chi_\Delta \to \chi^s_{K\Sigma^*} = \frac{2}{27}\, C^2, \qquad (24)$$

where the square of the strange-quark charge factor of $1/9$ is included in the coefficients.

In the next section, the lattice results are treated with partially quenched $\chi$EFT, i.e. using the coefficients in Eqs. (18), (19), (21), and (22). The full QCD coefficients can be recovered by keeping only the first term on the right-hand side of these equations. The effect of unquenching the missing light-quark disconnected loop contributions is investigated first, followed by a complete restoration of sea-quark-loop contributions through the inclusion of strange-quark-loop contributions in the kaon dressings.

## IV. CHIRAL EXTRAPOLATION

The finite-volume correction and chiral extrapolation of the magnetic polarizability of the neutron can now be performed with the lattice simulation results of Ref. [10]. The $2 + 1$ flavor simulation results are illustrated in Fig. 5 with a partially quenched finite-volume extrapolation suitable for these lattice results.

The extrapolation includes a term linear in $m_\pi^2$, with coefficient $a_2$ determined by a fit to the lattice results. The fit value of $a_2$ is small, at $6.5 \times 10^{-7}\text{fm}^5$. In illustrating the extrapolation curve, the results for $m_\pi L < 3$ are not shown, and it is noted that the magnetic polarizability at the physical point cannot be reached with a $(3\text{ fm})^3$ volume. Alternatively, one could apply the more conservative constraint of $m_\pi L > 4$ without changing the shapes of the extrapolation curves, as all lattice points used satisfy $m_\pi L > 4.45$. In Figs. 5, 6 and 8, the preference is to illustrate the results over a wider range.

Since the Sommer scale has been selected, the lattice volume varies slightly across the four lattice points
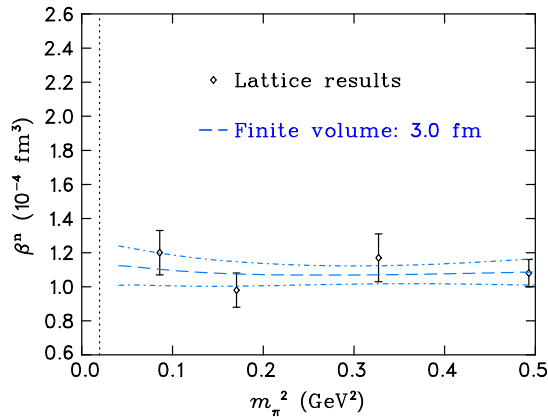
FIG. 5 (color online). Extrapolation of the magnetic polarizability of the neutron $\beta^n$ at spatial length $L = 3.0$ fm. The lattice points satisfy $m_\pi L > 3$. The dot-dashed curves indicate the error bar associated with the fit. The vertical dotted line indicates the physical point.
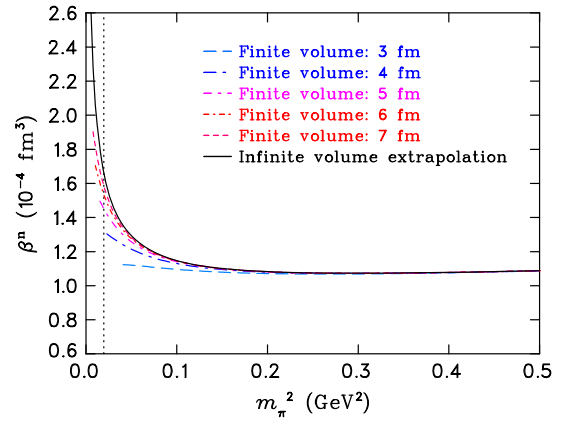
FIG. 6 (color online). Extrapolation of the magnetic polarizability of the neutron, $\beta^n$, for a variety of spatial lattice volumes, and the infinite volume limit.

available. However, the finite-volume corrections for large pion-mass values are relatively small, as illustrated in an example extrapolation for spatial length 3.0 fm, which corresponds to the volume of the lightest point at $m_\pi = 293$ MeV. Differences between the results for the varying volume and those for a 3.0 fm box at the higher pion-mass points are very small and cannot be seen in Fig. 5.

Chiral extrapolations for a range of finite volumes, and the infinite volume, are shown in Fig. 6. This highlights the manner in which the discretization of momenta to only those available on the finite volume significantly suppresses the chiral dressings of the neutron. The anticipated chiral curvature is significantly reduced on smaller lattice volumes. As precision lattice results become available, these curves can provide an important benchmark in understanding the volume dependence of those results.

For volumes of $(4\text{ fm})^3$ and larger, finite-volume corrections are significant only for $m_\pi < 300$ MeV, but they grow quickly in the chiral regime. Consequently, box sizes as large as 7 fm are required to obtain an extrapolation within 5% of the infinite-volume value at the physical point.

The effect of unquenching the disconnected loops by replacing the meson dressings of partially quenched QCD with those of full QCD is shown in Fig. 7 at infinite volume. One constrains the analytic terms, $a_0 + a_2 m_\pi^2$, of the chiral expansion by fitting the partially quenched chiral expansion to the partially quenched lattice simulation results corrected to infinite volume. The black curve of Fig. 7 illustrates this fit.

With the regulator parameter fixed to $\Lambda = 0.8$ GeV, the analytic terms model the invariant core contribution [40,51–55] to the polarizability. One can then correct the meson-cloud contribution by adding the valence-sea and sea-sea-loop integrals. Figure 7 illustrates the important effect of unquenching the light $u$ and $d$ sea-quark sector
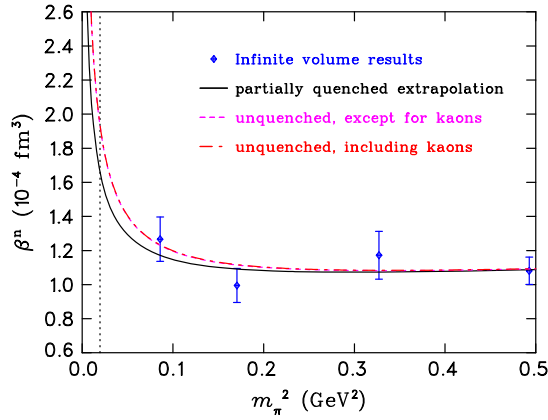
FIG. 7 (color online).   A comparison of the extrapolations of the magnetic polarizability of the neutron $\beta^n$, upon including the contributions of photon couplings to the disconnected $u$, $d$ and $s$ quark loops, which were omitted in the lattice QCD simulations.

contributions to the magnetic polarizability with the magenta dashed curve. The final effect of fully unquenching the results by also unquenching the strange sector through the addition of kaon loops is illustrated by the red dot-dashed curve.

The unquenched theory displays a significant increase in the strength of the chiral-loop integrals, with the value at the physical point sitting higher than in the partially quenched case. At the physical point, the magnetic polarizability is only $1.66 \times 10^{-4}$ fm$^3$, whereas the full theory provides $1.93 \times 10^{-4}$ fm$^3$, a 16% correction.

In contrast, unquenching the kaon loops has a very tiny effect, with a percentage shift of approximately 0.16%. This is significantly smaller than the effect of the strange-quark contributions to the proton magnetic moment [52] of 0.55%. Isolating the strange-quark/sea-sea contribution via
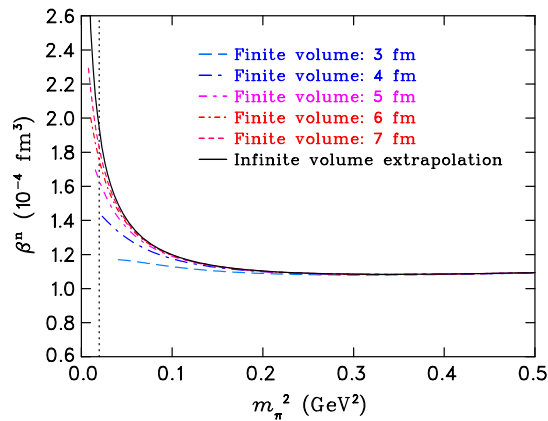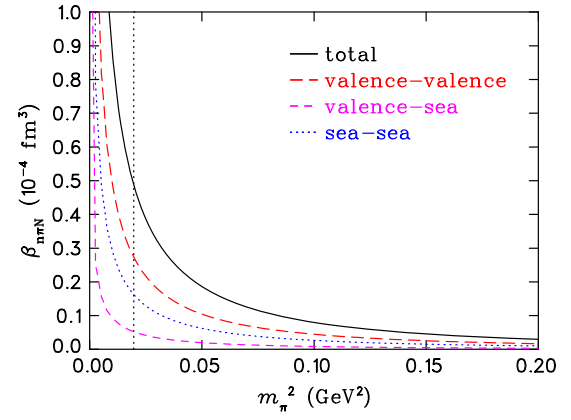


FIG. 9 (color online).   The contributions from separate photon-quark coupling scenarios to the leading-order octet loop integral of Eq. (6). In the valence-sea case where one photon couples to a valence quark and the other couples to a sea quark, there is a large positive contribution from $n \to K^0 \Lambda$, and the overall valence-sea result is positive.

Eqs. (23) and (24) provides a more closely related comparison of strange-sea-quark-loop contributions. In this case, the strange-sea-quark-loop contribution to the magnetic polarizability is $0.0023 \times 10^{-4}$ fm$^3$, a 0.12% contribution.

A comparison of multiple finite-volume and infinite-volume extrapolations for full QCD is shown in Fig. 8, correcting for partial-quenching effects. These results thus provide a benchmark to guide the interpretation of future lattice QCD simulations including background field effects in the disconnected sea-quark-loop sector.

The breakdown of the loop-integral contributions into the valence-valence, valence-sea, and sea-sea contributions is illustrated in Fig. 9 for the $\pi N$ sector of Eq. (6) and Fig. 10 for the $\pi \Delta$ sector of Eq. (7). The difference in the



FIG. 8 (color online).   Extrapolation of the unquenched value of $\beta^n$ for a variety of spatial lattice volumes, and the infinite volume case, correcting for partial quenching effects. These results provide a benchmark to guide the interpretation of future lattice QCD simulations, including background field effects in the disconnected sea-quark-loop sector.
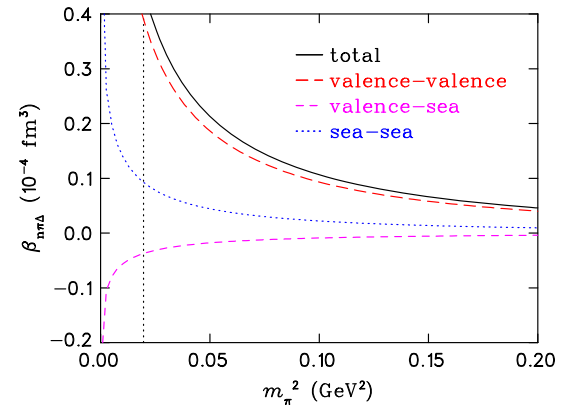


FIG. 10 (color online).   The contributions from separate photon-quark coupling scenarios to the next-to-leading-order decuplet loop integral of Eq. (7). In the valence-sea case, the negative contribution from $n \to K^+ \Sigma^*$ dominates, and the overall valence-sea result is negative.

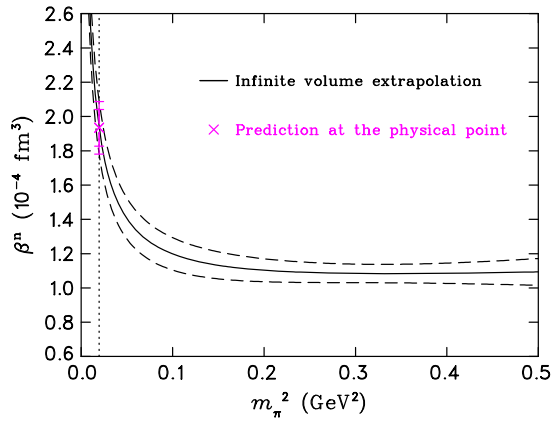FIG. 11 (color online). Our prediction for the pion-mass dependence of the magnetic polarizability of the neutron, $\beta^n$, is illustrated by the solid and dashed curves, illustrating combined statistical and systematic uncertainties. At the physical point, the inner error bar represents the statistical uncertainty from the fit to the lattice data, and the outer error bar adds the systematic uncertainty from the meson-cloud parameter, $\Lambda$, in quadrature.

sign of the valence-sea contribution between the two plots is noteworthy, as it highlights an important difference between the octet and decuplet processes. The quark-flow diagrams corresponding to a neutral intermediate ($n$ or $\Delta^0$) are the same, and the valence-sea contribution from each is negative due to the opposite charges of the $q\bar{q}$ pairs. However, in the case of the octet, the large contributions from $K^0\Lambda$-type coupling for the disconnected $u$-quark loop in the $n \to p\pi^-$ channel dominate over the similar $d$-quark loop in the neutral channel. The $\bar{u}$- and $d$-quark charges multiply positively, and the valence-sea contribution is positive. In the decuplet, there is no equivalent large coupling, and the neutral channel, $n \to \Delta^0\pi^0$, dominates, causing the valence-sea contribution to be negative.

The final infinite-volume full-QCD prediction for the magnetic polarizability of the neutron is shown in Fig. 11, with a value of $\beta^n = 1.93(11)(11) \times 10^{-4}$ fm$^3$ at the physical point. The quoted uncertainties represent both the statistical error from constraining the fit parameters to lattice QCD results and the systematic uncertainty from variation of $\Lambda$ over the range $0.7 \leq \Lambda \leq 0.9$. In the plot, the inner error bar represents the statistical uncertainty from the fit only, and the outer error bar includes the systematic uncertainty from the regulator parameter $\Lambda$ added in quadrature. Since the lattice results are obtained using a single lattice-spacing, it is not possible to quantify an uncertainty associated with taking the continuum limit. However, the lattice calculations are performed using a nonperturbatively improved clover-fermion action, and it is therefore anticipated that the $O(a^2)$ corrections are small relative to the uncertainties already addressed.

A comparison between our result and the experimental data is shown in Fig. 12. In addition to the Particle Data
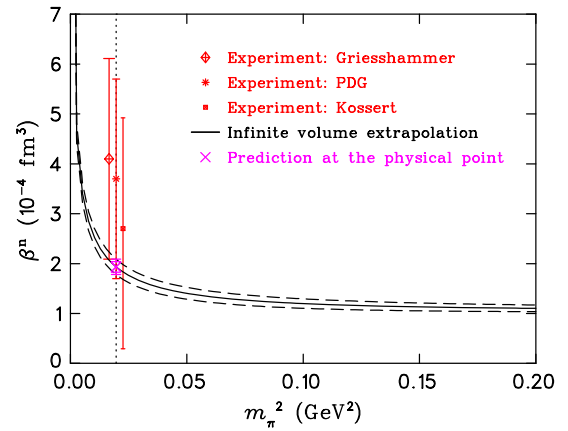


FIG. 12 (color online). The magnetic polarizability of the neutron $\beta^n$ is compared with experimental results. Uncertainties contain both statistical and systematic errors added in quadrature. Experimental results from Grießhammer *et al.* [6], the PDG [7], and Kossert *et al.* [3,4] are offset for clarity.

Group value [7], analyses of elastic photon-deuteron scattering experiments by Grießhammer *et al.* [6] and Kossert *et al.* [3,4] are included in the plot. For clarity of comparison, an $m_\pi^2$-axis offset is introduced among the experimental points. Our result is in good agreement with all three experimental measurements and presents an interesting challenge for greater precision in the experimental measurement. Such progress would similarly drive further progress in lattice QCD simulations and chiral effective field theory.

## V. CONCLUSION

Dynamical lattice QCD simulation results for the magnetic polarizability of the neutron have only recently become available [10]. The results are obtained at finite volume, and only the quarks carrying the quantum numbers of the hadron experience the background field. The dynamical fermion loops of the QCD simulation are blind to the external field. As such, it is timely to investigate the physics required to relate these new partially quenched simulation results to experiment.

Heavy baryon chiral effective field theory provides a framework in which to perform this investigation. Methods to correct for the finite volume of the spatial lattice volume are well established and employed herein. Techniques to unquench the sea-quark-loop contributions are also well established [40,51–53], but their application to the magnetic polarizability herein is novel.

This work has made definitive progress in providing a theoretical prediction for the magnetic polarizability of the neutron. We find $\beta^n = 1.93(11)^{\text{stat}}(11)^{\text{sys}} \times 10^{-4}$ fm$^3$. The prediction is founded on first-principles lattice QCD simulations and incorporates effective field theory techniques to correct for the finite volume of the lattice, account for the disconnected sea-quark-loop contributions, and

connect to the light-quark masses of nature. The result agrees with current experimental estimates and presents an interesting challenge for greater precision in the experimental measurement.

In performing the chiral extrapolations, the finite-volume effects were quantified for a range of spatial lattice volumes relevant to current and future lattice simulations. Both partially quenched and full QCD results were addressed in the finite-volume analysis. It was found that lattices of approximately 7 fm on a side are required to obtain the magnetic polarizability of the neutron to within 5% of the infinite-volume value at the physical pion mass. These finite-volume studies provide a benchmark for future lattice QCD calculations and a guide to the interpretation of the results.

Unquenching the disconnected loop contributions provides a significant increase in the chiral curvature of the magnetic polarizability and a significantly larger prediction at the physical point. Unquenching the $u$, $d$ and $s$ disconnected-loop contributions resulted in a 16% increase in the infinite-volume prediction. The contribution from kaon loops is negligibly small, at 0.16%. This is smaller than the 0.55% effect associated with strange-quark contributions to a proton's magnetic moment [52].

A more precise experimental measurement of the magnetic polarizabilities of the nucleon is clearly warranted. Similarly, further investment in lattice QCD investigations is of value. In the case of lattice QCD, the difficult problem of Landau-level contributions to the correlation functions is of interest, as is the need to directly incorporate sea-quark-loop effects. Finally, higher-order terms of the chiral expansion are valuable in evaluating the convergence of the effective field theory.

## ACKNOWLEDGMENTS

[1] J. Bernabeu, T. E. O. Ericson, and C. Ferro Fontan, Phys. Lett. **49B**, 381 (1974).

[2] V. Bernard, N. Kaiser, and U. G. Meissner, Phys. Rev. Lett. **67**, 1515 (1991).

[3] K. Kossert, M. Camen, F. Wissmann, J. Ahrens, H. Arends *et al.*, Phys. Rev. Lett. **88**, 162301 (2002).

[4] K. Kossert, M. Camen, F. Wissmann, J. Ahrens, J. Annand *et al.*, Eur. Phys. J. A **16**, 259 (2003).

[5] J. McGovern, D. Phillips, and H. Griesshammer, Eur. Phys. J. A **49**, 12 (2013).

[6] H. Grießhammer, J. McGovern, D. Phillips, and G. Feldman, Prog. Part. Nucl. Phys. **67**, 841 (2012).

[7] J. Beringer *et al.* (PDG), Phys. Rev. D **86**, 010001 (2012).

[8] B. Tiburzi and S. Vayl, Phys. Rev. D **87**, 054507 (2013).

[9] T. Primer, W. Kamleh, D. Leinweber, and M. Burkardt, *Proc. Sci.*, LATTICE2012 (**2012**) 183.

[10] T. Primer, W. Kamleh, D. Leinweber, and M. Burkardt, Phys. Rev. D **89**, 034508 (2014).

[11] J. Hall, D. Leinweber, and R. Young, Phys. Rev. D **85**, 094502 (2012).

[12] J. Hall, D. Leinweber, B. Owen, and R. Young, Phys. Lett. B **725**, 101 (2013).

[13] J. Hall, D. Leinweber, and R. Young, Phys. Rev. D **88**, 014504 (2013).

[14] L. Greil, T. R. Hemmert, and A. Schafer, Eur. Phys. J. A **48**, 53 (2012).

[15] M. Albaladejo, J. Oller, E. Oset, G. Rios, and L. Roca, J. High Energy Phys. 08, (2012) 071.

[16] M. Doring, M. Mai, and U.-G. Meissner, Phys. Lett. B **722**, 185 (2013).

[17] R. A. Briceno, Z. Davoudi, and T. C. Luu, Phys. Rev. D **88**, 034502 (2013).

[18] S. Boinepalli, D. Leinweber, A. Williams, J. Zanotti, and J. Zhang, Phys. Rev. D **74**, 093005 (2006).

[19] S. Aoki *et al.* (PACS-CS Collaboration), Phys. Rev. D **79**, 034503 (2009).

[20] R. Kenway, *The Logic of Nature, Complexity and New Physics: From Quark-Gluon Plasma to Superstrings, Quantum Gravity and Beyond* , The Subnuclear Series Vol. **44** (World Scientific, Singapore, 2008) p. 137.

[21] S. Collins, M. Gockeler, P. Hagler, R. Horsley, Y. Nakamura *et al.*, Phys. Rev. D **84**, 074507 (2011).

[22] C. Bouchard, G. P. Lepage, C. Monahan, H. Na, and J. Shigemitsu, Phys. Rev. D **88**, 054509 (2013).

[23] S. Prelovsek, L. Leskovec, C. Lang, and D. Mohler, Phys. Rev. D **88**, 054508 (2013).

[24] S. Aoki, Y. Aoki, C. Bernard, T. Blum, G. Colangelo *et al.*, arXiv:1310.8555.

[25] T. Inoue, S. Aoki, T. Doi, T. Hatsuda, Y. Ikeda, N. Ishii, K. Murano, H. Nemura, and K. Sasaki (HAL QCD Collaboration), Phys. Rev. Lett. **111**, 112503 (2013).

[26] D. B. Leinweber, A. W. Thomas, and R. D. Young, Phys. Rev. Lett. **92**, 242002 (2004).

[27] D. B. Leinweber, A. W. Thomas, and R. D. Young, Nucl. Phys. **A755**, 59 (2005).

[28] J. M. M. Hall, D. B. Leinweber, and R. D. Young, Phys. Rev. D **82**, 034010 (2010).

[29] J. M. M. Hall, F. X. Lee, D. B. Leinweber, K. F. Liu, N. Mathur, R. D. Young, and J. B. Zhang, Phys. Rev. D **84**, 114011 (2011).

[30] M. G. Beckett, P. Coddington, B. Joó, C. M. Maynard, D. Pleiter, O. Tatebe, and T. Yoshie, Comput. Phys. Commun. **182**, 1208 (2011).

[31] W. Detmold, B. Tiburzi, and A. Walker-Loud, Phys. Rev. D **73**, 114505 (2006).

[32] C. W. Bernard, T. Draper, K. Olynyk, and M. Rushton, Phys. Rev. Lett. **49**, 1076 (1982).

[33] J. Smit and J. C. Vink, Nucl. Phys. **B286**, 485 (1987).

[34] M. Burkardt, D. B. Leinweber, and X. Jin, Phys. Lett. B **385**, 52 (1996).

[35] F. Lee, R. Kelly, L. Zhou, and W. Wilcox, Phys. Lett. B **627**, 71 (2005).

[36] F. X. Lee, L. Zhou, W. Wilcox, and J. C. Christensen, Phys. Rev. D **73**, 034503 (2006).

[37] F. X. Lee, S. Moerschbacher, and W. Wilcox, Phys. Rev. D **78**, 094502 (2008).

[38] R. Sommer, Nucl. Phys. **B411**, 839 (1994).

[39] P. Wang, D. B. Leinweber, A. W. Thomas, and R. D. Young, Phys. Rev. D **75**, 073012 (2007).

[40] P. Wang, D. Leinweber, A. Thomas, and R. Young, Phys. Rev. D **79**, 094001 (2009).

[41] V. Lensky and V. Pascalutsa, Eur. Phys. J. C **65**, 195 (2010).

[42] W. Armour, C. R. Allton, D. B. Leinweber, A. W. Thomas, and R. D. Young, J. Phys. G **32**, 971 (2006).

[43] J. Hall, A. C. P. Hsu, D. Leinweber, A. Thomas, and R. Young, Phys. Rev. D **87**, 094510 (2013).

[44] V. Bernard, N. Kaiser, and U. G. Meissner, Nucl. Phys. **B373**, 346 (1992).

[45] V. Bernard, N. Kaiser, A. Schmidt, and U. G. Meissner, Phys. Lett. B **319**, 269 (1993).

[46] V. Bernard, N. Kaiser, U. G. Meissner, and A. Schmidt, Z. Phys. A **348**, 317 (1994).

[47] A. Ali Khan et al. (QCDSF-UKQCD), Nucl. Phys. **B689**, 175 (2004).

[48] S. R. Beane, Phys. Rev. D **70**, 034507 (2004).

[49] J. M. Hall and V. Pascalutsa, Eur. Phys. J. C **72**, 2206 (2012).

[50] J. M. Hall, D. B. Leinweber, and R. D. Young, AIP Conf. Proc. **1354**, 78 (2011).

[51] R. D. Young, D. B. Leinweber, A. W. Thomas, and S. V. Wright, Phys. Rev. D **66**, 094507 (2002).

[52] D. B. Leinweber, S. Boinepalli, I. Cloet, A. W. Thomas, A. G. Williams, R. Young, J. Zanotti, and J. Zhang, Phys. Rev. Lett. **94**, 212001 (2005).

[53] D. B. Leinweber, S. Boinepalli, A. W. Thomas, P. Wang, A. G. Williams, R. Young, J. Zanotti, and J. Zhang, Phys. Rev. Lett. **97**, 022001 (2006).

[54] P. Wang, D. Leinweber, A. Thomas, and R. Young, Phys. Rev. C **79**, 065202 (2009).

[55] P. Wang, D. Leinweber, and A. Thomas, Phys. Rev. D **89**, 033008 (2014).

[56] D. B. Leinweber, Phys. Rev. D **69**, 014005 (2004).